

Robust Estimation of Field Inhomogeneity Map Following Magnitude-Based Water-Fat Separation with Resolved Ambiguity

Alexandre Triay Bagur^{1,2*}, Darryl McClymont², Chloe Hutton², Andrea Borghetto², Michael L Gyngell², Paul Aljabar², Matthew D Robson², Michael Brady², Daniel P Bulte¹

¹Department of Engineering Science, University of Oxford, Oxford, UK

²Perspectum Ltd, Oxford, UK

* Corresponding author. Email: alexandre.triaybagur@eng.ox.ac.uk

Running Title: Fieldmap Estimation Following Magnitude Water-Fat Separation

Word Count: 4704

Data Availability Statement: Publicly available 1.5 T data from the UK Biobank study was analyzed in this work. The UK Biobank datasets are available to researchers through an open application via <https://www.ukbiobank.ac.uk/register-apply/>. The additional 3 T dataset used in this study was de-identified and uploaded to Zenodo under <https://doi.org/10.5281/zenodo.6652300>.

Acknowledgement: The authors thank the Engineering and Physical Sciences Research Council (EPSRC) for funding via a doctoral studentship (project reference 2280970). This research has been conducted using the UK Biobank Resource under application 9914. This publication is our view, and the Executive Agency for Small and Medium-sized Enterprises is not responsible for any use of the information herein.

Abstract

PURPOSE: To extend magnitude-based PDFF (Proton Density Fat Fraction) and R_2^* mapping with resolved water-fat ambiguity to calculate field inhomogeneity (field map) using the phase images.

THEORY: The estimation is formulated in matrix form, resolving the field map in a least-squares sense. PDFF and R_2^* from magnitude fitting may be updated using the estimated field maps.

METHODS: The limits of quantification of our voxel-independent implementation were assessed. Bland-Altman was used to compare PDFF and field maps from our method against a reference complex-based method on 152 UK Biobank subjects (1.5 T Siemens). A separate acquisition (3 T Siemens) presenting field inhomogeneities was also used.

RESULTS: The proposed field mapping was accurate beyond double the complex-based limit range. High agreement was obtained between the proposed method and the reference in UK Biobank (PDFF bias = -0.03 %, LoA (limits of agreement) [-0.1,0.1] %; Field map bias = 0.06 Hz, LoA = [-0.2,0.3] Hz). Robust field mapping was observed at 3 T, for inhomogeneities over 300 Hz including rapid variation across edges.

CONCLUSION: Field mapping following magnitude-based water-fat separation with resolved water-fat ambiguity was demonstrated in-vivo and showed potential at high field.

Keywords

Proton density fat fraction, MRI-PDFF, fat-water swap, quantitative susceptibility mapping

Introduction

Chemical-shift encoded (CSE) MRI water-fat separation methods have emerged as non-invasive tools for proton density fat fraction (MRI-PDFF or PDFF) and R_2^* ($1/T_2^*$) quantification. PDFF has been applied successfully in non-alcoholic steatohepatitis (NASH) drug trials as a replacement for a liver biopsy for the detection of steatosis¹. Beyond the liver, PDFF has been proposed as an imaging biomarker in the heart, muscle, pancreas, kidney, and adipose tissue deposits^{2,3}. R_2^* has shown utility in the quantification of liver iron content (LIC)⁴.

The majority of advanced CSE algorithms, such as Iterative Decomposition of Water and Fat with Echo Asymmetry and Least-Squares Estimation (IDEAL)⁵ and Variable Projection (VARPRO)⁶, are complex-based, in the sense that they require both the MRI magnitude and phase images as input. Complex-based CSE estimates fat and water proportions indirectly through the estimation of B_0 field inhomogeneity, conventionally referred to as the “field map”. Each field map value leads to a unique solution for water and fat proportions within a voxel^{5–7}. However, this implies dependence of water and fat estimation on accurate field map estimation. Importantly, field mapping is a nonconvex optimization problem with many local minima^{7,8}. Erroneous field map convergence leads to incorrect PDFF and R_2^* quantification, and may manifest as fat-water swaps in the PDFF images⁷. Spatial smoothness constraints are often imposed on the field map to regularize the optimization, for instance through using region-growing^{7,9}, Markov Random Fields (MRF)^{6,10}, or graph cuts^{8,11–13}. These methods have been shown to work well under a range of scanning conditions and anatomies^{12,14}. However, the imposed smoothness constraints may be inappropriate, for instance depending on the magnetic susceptibility of the object, or in transition regions with high field inhomogeneity, causing over-smoothing of PDFF and compromising any downstream quantification.

CSE methods that use only the magnitude of the MRI source images, which we refer to as magnitude-based, have also been proposed¹⁵. Magnitude-based methods do not require field map estimation prior to water-fat separation and are unaffected by errors in phase images due, for example, to eddy currents. In practice, complex-based methods are often subject to a final magnitude fitting step to correct phase errors in water and fat images, an approach that has been dubbed “hybrid” estimation¹⁶. Magnitude-based methods optimize water and fat (and thus PDFF) directly but have tended to suffer from water-fat ambiguity, meaning they could not identify the dominant species within a voxel (water or fat), which, it was believed, limited the dynamic range of PDFF to 0 to 50%^{1,15,17}. A recently proposed method, MAGnitude-Only (MAGO)¹⁸, exploits the spectral complexity of fat to unambiguously identify the dominant species and thus estimate PDFF over the entire 0-100% range¹⁸. MAGO has been shown to give excellent accuracy and reproducibility across manufacturers and clinical field strengths, in simulations, phantoms and in-vivo studies¹⁸. Recently an extension to MAGO which accounts for the

Rician noise distribution in magnitude-only MRI data, MAGORINO, has been proposed, provided accurate noise characterization is performed¹⁹.

Though, under the MAGO framework, field map estimation is not required for full-range PDFF and accurate R_2^* estimation, the field map may still be useful to assess image quality or, importantly, in the context of quantitative susceptibility mapping (QSM)²⁰, where the field map is subsequently decomposed into a local component and a background component. QSM has been successfully applied in the abdomen for measurement of liver iron content²⁰.

In this study, we demonstrate field mapping from complex-valued data following magnitude-based water-fat separation and PDFF estimation where the water-fat ambiguity has been resolved using MAGO. The method is described using theory and simulations. The method is first validated against a state-of-the-art regularized complex-based method in a cohort from the UK Biobank imaging sub-study (1.5 T), which show low field inhomogeneity. The method is then applied to a 3 T acquisition with high field inhomogeneities, including rapid field transitions.

Theory

Signal Models

PDFF fitting conventionally uses the following generalized signal model at each pixel, which is not made explicit to simplify the notation:

$$s_n = (\rho_W + \rho_F C_n) e^{i(2\pi f_B t_n + \phi_0)} e^{-R_2^* t_n} \quad \text{Equation 1}$$

where $s_n = s(t_n)$ is the observed signal at echo time t_n , where there are a total of N echoes $[t_1, t_2, \dots, t_N]$, ρ_W is the unknown water magnitude and ρ_F is the unknown fat magnitude, and f_B is the frequency shift due to local field inhomogeneities or “field map” ($2\pi f_B$ is sometimes expressed as ψ). The term $C_n = \sum_{p=1}^P \alpha_p e^{i2\pi f_p t_n}$ addresses the multi-frequency nature of the fat species, where α_p and f_p are the relative amplitudes and relative frequencies of the spectral model of fat with P peaks. The 6-peak liver model is assumed in this work²¹. This signal model is phase-constrained^{22–24}, meaning that

water and fat share the same initial phase $\phi_W = \phi_F = \phi_0$, which is a reasonable assumption in spoiled gradient echo acquisitions²⁵, and provides noise performance advantages²³.

When fitting only the magnitude of the signal, the model becomes

$$|s_n| = |\rho_W + \rho_F C_n| e^{-R_2^* t_n} \quad \text{Equation 2}$$

where $|x|$ denotes the modulus. Note that the exponential term contributes only to the phase information, $e^{i(2\pi f_B t_n + \phi_0)}$, has unit modulus, and is dropped. It follows that magnitude-based methods avoid computing both the field map f_B and the initial phase term ϕ_0 . Finally, PDFF may be computed using the water and fat magnitudes using the ratio

$$\text{PDFF} = \frac{\rho_F}{\rho_W + \rho_F} \times 100 \text{ (\%)} \quad \text{Equation 3}$$

Magnitude Fitting with Resolved Water-Fat Ambiguity

MAGO reported that spectral complexity and multipoint optimization helps resolve the water-fat ambiguity of magnitude methods, enabling full-range PDFF estimation¹⁸. MAGO is confounder-corrected for a composite fat spectrum, R_2^* relaxation and phase errors. In MAGO, at each voxel the magnitude signal equation above is solved twice using nonlinear optimization from two different starting points, one near 0% PDFF, the other near 100% PDFF¹⁸, obtaining the candidate solution sets $\{\rho_W, \rho_F, R_2^*\}_1$ and $\{\rho_W, \rho_F, R_2^*\}_2$. The solution chosen by MAGO at each voxel, $\{\rho_W, \rho_F, R_2^*\}$, is the one with lower associated fitting residual. The ‘alternative’ solution will be chosen as the candidate solution set with the higher associated fitting residual, where fat and water will be ‘swapped’. This enables accurate PDFF estimation from 0% to 100%. The ‘alternative’ solution may be kept to further refine PDFF and R_2^* , as described in the next sections.

Figure 1 shows an illustration of the chosen MAGO solution set and the alternative MAGO solution set. The chosen solution set contains at each voxel the Water, Fat, PDFF and R_2^* values with lower associated fitting residual (better fit). The alternative solution set contains at each voxel the Water, Fat, PDFF and R_2^* values with higher associated fitting residual (worse fit).

Proposed Voxel-Independent B_0 Field Estimation using Full-Range PDFF and R_2^*

The chosen full-range magnitude-based solution set from MAGO, $\{\rho_W, \rho_F, R_2^*\}$, may be used to guide field map f_B (and initial phase ϕ_0) reconstruction using the source complex-valued data. To this end, we explore whether prior knowledge about water, fat and R_2^* may be useful for estimating the field map.

For given values of water, fat and R_2^* , the following terms of the complex-based signal model in Equation 1 are known: $\varrho_n \equiv (\rho_W + \rho_F C_n)$ and $R_n \equiv e^{-R_2^* t_n}$, which may be rearranged to yield the simplified expression:

$$\frac{s_n}{\varrho_n R_n} = e^{j(2\pi f_B t_n + \phi_0)}$$

This implies that the field map f_B and the phase offset ϕ_0 can be estimated given ρ_W , ρ_F , R_2^* and using the input complex-valued data s_n . Taking the phase from both sides,

$$P_n = \arg\left(\frac{s_n}{\varrho_n R_n}\right) = 2\pi f_B t_n + \phi_0 + 2\pi k \quad \text{Equation 4}$$

with k an integer, then the estimation may be formulated as a linear equation in matrix form,

$$\mathbf{P} = \begin{bmatrix} P_1 \\ \vdots \\ P_N \end{bmatrix} = \begin{bmatrix} 2\pi t_1 & 1 \\ \vdots & \vdots \\ 2\pi t_N & 1 \end{bmatrix} \begin{bmatrix} f_B \\ \phi_0 \end{bmatrix} = \mathbf{A} \boldsymbol{\varphi} \quad \text{Equation 5}$$

where $\boldsymbol{\varphi} = [f_B, \phi_0]^T$ are unknowns, and \mathbf{A} is a $N \times 2$ matrix where the first column vector contains the echo times and the 2π term, $[2\pi t_1, 2\pi t_2, \dots, 2\pi t_N]^T$, and the second column contains ones $[1, 1, \dots, 1]^T$. This makes for a computationally efficient estimation.

For each pixel in the source image, the proposed algorithm first creates the ϱ_n and R_n terms using the MAGO chosen solution set $\{\rho_W, \rho_F, R_2^*\}$, the echo times and the 6-peak spectral model of fat. Then, the input complex-valued data s_n is divided by the $\varrho_n R_n$ term, $s_n/(\varrho_n R_n)$. The phase of the output is taken and unwrapped in *the echo times' dimension* (rather than in the spatial dimensions), by changing absolute jumps greater than π to their 2π complement starting from the first echo time. The echo times' matrix \mathbf{A} is then defined and used to find a least squares solution to the linear equation system in Equation 5.

For correction in the presence of bipolar gradients that create an additional phase shift to the signal $(-1)^n \theta^{26}$, one may reformulate Equation 5 to estimate three unknowns, $\boldsymbol{\varphi}' = [f_B, \phi_0 - \theta, \phi_0 + \theta]^T$, namely the combination of the common phase offset of water and fat, ϕ_0 , and a phase offset due to bipolar gradient effects, θ , with opposite sign for odd and even echoes. In this scenario, the echo times matrix \mathbf{A}' may be defined as a $N \times 3$ matrix as follows (for even N):

$$\mathbf{A} = \begin{pmatrix} 2\pi t_1 & 1 & 0 \\ 2\pi t_2 & 0 & 1 \\ \vdots & \vdots & \vdots \\ 2\pi t_N & 0 & 1 \end{pmatrix}$$

This approach enables parameter sharing of the bipolar gradients term and the initial phase offset, which may be disentangled further into ϕ_0 and θ . Disentangling into ϕ_0 and θ was out of the scope of this work as these two terms are often considered unimportant²².

We may additionally estimate f_B and ϕ_0 using this approach for the MAGO *alternative* solution set as well, which may provide a basis to refine the MAGO PDFF and R_2^* maps. One proposed implementation of such refinement is described in the Methods section.

B₀ Field Cost Function: $R(f_B)$

The overall residual of the signal model may be plotted against the field map, for visual assessment of the cost (or loss) function $R(f_B)^{7-9}$. For voxel-independent iterative complex-based estimation, for instance the IDEAL approach⁵ with R_2^* decay and multi-peak fat spectrum modelling²⁷, the field map f_B may be estimated by minimizing the residual loss function $R_C(f_B)$:

$$R_C(f_B) = \|[R_1, R_2, \dots, R_N]\|_2^2 = \sum_{n=1}^N (s_n - \hat{s}_n)^2$$

where \hat{s}_n is the noiseless signal equation using the estimated values $\{\widehat{\rho}_W, \widehat{\rho}_F, \widehat{f}_B, \widehat{R}_2^*\}$. For our proposed estimation method, where full-range magnitude-based estimates are used as inputs, the residual loss function to minimize is based on Equation 5:

$$R_M(f_B) = \|\mathbf{P} - \mathbf{A} \boldsymbol{\varphi}\|_2^2$$

Figure 2 plots the cost functions for the complex-based formulation, $R_C(f_B)$, and for our proposed formulation, $R_M(f_B)$, within a voxel; the former replicates Figure 1a in Yu et al.⁷, but with the addition of R_2^* decay, 6-peak fat spectrum modelling²¹, and evenly spaced echo times (3 echoes, $TE_1=2$ ms, $\Delta TE=2$ ms). For the particular case of uniformly spaced echo times, the cost function is periodic with period $1/\Delta TE$ ^{8,9}. The loss function curves were simulated over the field map range -1000 to 1000 Hz at 1.5 T (imaging frequency = 64 MHz), using the true values of water, fat and R_2^* . The cost functions were plotted for varying water:fat proportions, namely 4:1, 2:1, 1:1, and 1:2.

Voxel-independent IDEAL estimation wrongly converges to a local minimum (‘aliased’ solution) when the true field map value is beyond approximately $\pm\Delta f/2$, where Δf is the off-resonance frequency of the main fat peak relative to water ($\Delta f \approx 220$ Hz at 1.5 T), as described previously^{7,8}. The voxel-independent VARPRO implementation has been reported to produce equivalent results to voxel-independent IDEAL, because ambiguities are dealt with by forcing the field map to be within $\pm\Delta f/2$ ⁸. Such erroneous convergence may lead to fat-water swapping in the PDF map⁷.

Conversely, the proposed field mapping converges accurately with starting estimates beyond the $\pm\Delta f/2$ range for the same simulated data. Note that our formulation reduces the number of local minima in the search space compared to complex-based field mapping methodologies such as IDEAL, which need to deal with ambiguities relating to water and fat proportions. The proposed formulation is independent of water:fat proportion because the water-fat ambiguity is dealt with at the MAGO stage, and the water and fat signals are demodulated from the source data before field mapping is performed.

Methods

MRI Data

Datasets from N=152 nominally healthy UK Biobank (www.ukbiobank.ac.uk) volunteers were gathered, obtained using a Siemens Magnetom Aera 1.5 T scanner (Siemens Healthineers, Erlangen, Germany) with a two-dimensional single-slice, 10 mm slice thickness, 6-echo ($TE_1=1.2$ ms, $\Delta TE=2$ ms) gradient-recalled echo (GRE) protocol designed to minimize T1 bias (5° flip angle). UK Biobank is approved by the North West Multi-Centre Research Ethics Committee, and prior written consent was obtained from all participants. Liver segmentation masks were available from these subjects, that had been obtained using a deep learning-based liver segmentation model²⁸.

One other dataset was gathered using a Siemens Prisma 3 T scanner on a healthy volunteer to test the method under more a challenging field inhomogeneity range. Informed consent was obtained from the participant. The acquisition comprised thirty-two slices including the dome of the liver, heart, and lungs.

The acquisition consisted of a 6-echo ($TE_1=1.3$ ms, $\Delta TE=1$ ms) gradient-recalled echo (GRE) protocol designed to minimize T1 bias (3° flip angle), Pixel Bandwidth = 1565 Hz, and 232 x 256 reconstructed image size, with 5 mm slice thickness and 1.72×1.72 mm² in-plane resolution.

Overview of the Proposed Methodology

An overview of the proposed methodology is shown in Figure 3 and compared with state-of-the-art complex-based water-fat separation pipelines. Complex-based methods perform the following: (1) regularized B_0 field mapping; (2) complex-based estimation using the estimated field map, that yields unique PDFF and R_2^* maps; and (3) magnitude-based refinement of PDFF to correct for phase errors. In ‘mixed’ magnitude/complex fitting²⁹, steps 2 and 3 are performed simultaneously, but are in practice initialized with a regularized field map from step 1.

For this work, a state-of-the-art complex-based method was implemented as reference for comparison, which combined the method GLOBally Optimal Surface Estimation (GOOSE)¹² for step 1, and the method Hybrid T2*-IDEAL¹⁶, hIDEAL, for steps 2 and 3. GOOSE is among the top performing methods in the 2012 ISMRM Challenge datasets, with a mean score of 99.27¹², and is openly available. This method is referred to as GOOSE:hIDEAL throughout this work.

In our methodology, full-range PDFF estimation is performed regardless of whether phase data is available or reliable via the MAGO method¹⁸. Then, when phase data is available and (sufficiently) reliable, the proposed field mapping method may be used. To this point, the proposed method may run independently at each voxel. This is referred to as *proposed voxel-independent field mapping* throughout this work. The field map may be further adjusted and used to refine the PDFF and R_2^* maps from MAGO, as described in the next section.

Proposed Adjustment of Voxel-Independent Field Map and PDFF and R_2^*

Adjustment of the voxel-independent field map may be performed, which allows for the refinement of the PDFF and R_2^* maps from MAGO. First, the voxel-independent field maps are computed (using the *proposed voxel-independent field mapping* method) for both the chosen MAGO solution set and the alternative MAGO solution set, obtaining f_B^c and f_B^a , respectively. Then, the adjusted field map may be created by selecting, at each voxel, f_B^c or f_B^a , whichever is closest to a ‘smoothed’ version of f_B^c , $v(f_B^c)$. If f_B^a and $v(f_B^c)$ are closer than f_B^c and $v(f_B^c)$ are, then the chosen and alternative solution sets are switched for that voxel. This step yields an adjusted field map as well as adjusted PDFF and R_2^* maps,

because the whole solution set is consistently kept in the selection. In this work, median filtering with kernel size of 15-by-15 neighborhood was used to create $v(f_B^c)$.

This adjustment step was tested under simulated noisy conditions, described in the next section. The 3 T dataset was run with both the *proposed voxel-independent field mapping* method and with the *proposed adjusted field mapping* method for comparison.

Simulations

A slowly-varying synthetic field map was applied to one UK Biobank subject to explore the observation from Theory illustrated in Figure 2. The water magnitude, fat magnitude, and R_2^* outputs from⁷ GOOSE:hIDEAL were used to synthesize complex-valued echo images with the synthetic field map and an arbitrary initial phase offset of $\pi/4$ rad for the whole image. The synthetic field map was set to vary linearly starting from the center of the image. The same echo times from the original dataset were used in the simulation, as well as the 6-peak fat model. The synthesized complex-valued echo data was reconstructed with voxel-independent hIDEAL, as well as voxel-independent MAGO followed by the proposed voxel-independent field mapping.

One other simulation was performed to test the performance of the proposed adjustment of the field map at refining the MAGO PDFF and R_2^* maps under varying noise levels. The UK Biobank subjects were used for this experiment. For each subject, additive complex Gaussian noise was progressively applied to the echo images. At each noise level, the Signal-to-Noise Ratio (SNR) was measured from the first echo magnitude image, by taking the median signal within the liver over the median signal in the background. The process stopped when SNR was brought down to 5. PDFF and field map were estimated at each noise level using (1) the proposed voxel-independent implementation of field mapping, and (2) the proposed field map adjustment step with PDFF and R_2^* refinement. For each noise level, the percentage of ‘swapped’ liver voxels was computed by comparing the output PDFF map with a reference PDFF from GOOSE:hIDEAL that had been computed using the original data with no added noise. ‘Swapped’ voxels were defined according to Berglund and Skorpil¹¹, i.e. those with an absolute PDFF difference higher than 10% *and* with the opposite dominant species compared to the reference.

In-Vivo Evaluation

The proposed voxel-independent field mapping and the proposed field mapping with adjustment were demonstrated in the UK Biobank datasets and the thirty-two-slice dataset described earlier.

The 152 UK Biobank subjects were used to validate the proposed methods for *in vivo* agreement with state-of-the-art complex-based methodology under low B_0 field inhomogeneities. The UK Biobank subjects were processed using GOOSE:hIDEAL for PDFF and field map estimation, which served as reference, and also using the proposed methods. Median PDFF and field map values within the liver segmentation masks were extracted. The proposed methods' field map and PDFF medians were assessed against GOOSE:hIDEAL using Bland-Altman analysis³⁰.

The thirty-two-slice 3 T dataset was reconstructed using the proposed adjusted method and GOOSE:hIDEAL for reference. Bipolar gradients' correction was run for the proposed method as described in the Theory section. Information from neighboring slices was not used for any of the methods for a fair comparison.

Results

Simulations

Figure 4 shows the UK Biobank subject with the additional synthetic field map, reconstructed using the voxel-independent hIDEAL method and with the proposed voxel-independent method. In accordance with the observations from Figure 2, the voxel-independent hIDEAL method erroneously converges to an aliased solution beyond an initial field map value that is beyond the true field $\pm\Delta f/2$ (with $\Delta f \approx 220$ Hz at 1.5T). This results in fat-water swaps in the PDFF map. Consistently with Figure 2 also, the proposed voxel-independent field mapping enables estimation of field map beyond the $\pm\Delta f/2$ range, up to slightly beyond $\pm\Delta f$. Note the wraps in the field map from the proposed method do not affect PDFF, since field map estimation is performed after PDFF is obtained, unlike in the complex-based scenario, where PDFF estimation depends on field map convergence.

Figure 5 shows the performance of the proposed field map adjustment step on the UK Biobank population, where each subject was reconstructed under progressive noise. Performance was measured using the percentage of liver voxels that were 'swapped' compared to a reference PDFF computed with GOOSE:hIDEAL under no added noise. The proposed field map adjustment step keeps the percentage of 'swapped' voxels under 5% for all SNR levels down to 5. When taking summary metrics robust to outliers, such as the median, it is expected that 5% of pixels will have very little contribution to the reported value (see the In-Vivo Evaluation section). Conversely, the proposed voxel-independent implementation exceeds 5% of 'swapped' voxels for SNR near 10. Overall, for typical SNR in the liver in 1.5 T acquisitions (containing at least 6 echoes for accurate R_2^* relaxometry), SNR = 40, the adjustment step shows modest improvement in percentage of 'swapped' voxels the voxel-independent result.

Figure 6 shows the field map adjustment procedure with refinement of the MAGO PDFF map for a simulated SNR of 10 in one UK Biobank subject. The field map adjustment step is able to ‘unswap’ the majority of pixels, importantly within the liver, and render a solution that is comparable to the reference PDFF map from the original data with no added noise.

In-Vivo Evaluation

Figure 7 shows Bland-Altman comparisons of median PDFF and median field map values within the liver for the proposed methods against the reference GOOSE:hIDEAL, using the UK Biobank subjects. Voxel-independent hIDEAL results are also included for comparison. For PDFF quantification, a small bias of -0.03 % PDFF and a low variability of [-0.1, 0.1] % PDFF were observed for the proposed adjusted method, with overall excellent agreement with the reference. For field map quantification, a small bias of 0.06 Hz and a low variability of [-0.2, 0.3] Hz were observed for the proposed adjusted method, with overall excellent agreement with the reference. Voxel-independent hIDEAL showed comparable bias of 0 % but higher limits of agreement of [-0.2, 0.2] % for PDFF, and higher bias of 0.60 Hz and higher limits of agreement of [-5.8, 7.0] Hz for field map analysis.

Figure 8 shows one subject from the UK Biobank for four reconstruction methods: reference GOOSE:hIDEAL, voxel-independent hIDEAL, proposed voxel-independent field mapping, and the proposed adjusted field mapping. Note that, for the proposed methods, field mapping follows PDFF estimation, rather than the opposite. As can be observed, the proposed field mapping methods produce results that are comparable to the GOOSE:hIDEAL algorithm. Voxel-independent hIDEAL suffers from field map aliasing posteriorly in the liver and part of the subcutaneous fat and near the spleen, that result in fat-water swaps on the PDFF map, including a ‘double-swap’ within the liver (double swaps yield reasonable PDFF values, which may lead to misdiagnosis if not properly identified⁷). The proposed adjusted method is able to unswap a few voxels within the liver that were misidentified using the proposed voxel-independent method.

Figure 9 shows the six of the thirty-two slices from the 3 T dataset with liver coverage, processed using the proposed adjusted method and GOOSE:hIDEAL. Magnitude images from the first echo time are shown for anatomical reference. Field maps and water-separated images are shown for the two methods run. The scan shows both high field inhomogeneities overall as well as rapid field transitions near edges of organs, for example the dome of the liver or the spleen. Though no ground truth field maps or PDFF maps are available, the slice-by-slice variation in field map and PDFF is expected to be monotonic with increasing inhomogeneity further away from the isocenter. The slice-by-slice increase in the field maps by the proposed method was consistent and generally in agreement with GOOSE:hIDEAL. Some inconsistencies were observed near the arms for GOOSE:hIDEAL, which resulted in fat-water swaps.

No substantial fat-water swaps were observed for our method. Figure S1 and Figure S2 in the Supplementary Material show reconstruction using several other widely used methods from the literature, as well as the proposed voxel-independent method.

Discussion

This work demonstrated field mapping after magnitude-based water-fat separation with resolved water-fat ambiguity (MAGO). The proposed method is efficient and of relatively simple implementation. The method in its voxel-independent form doubled the traditional range limit of voxel-independent complex-based methods. Simulations demonstrated noise performance of the proposed method with adjustment. PDFF and field mapping were validated for accuracy with a regularized complex-based reference in simulated data and in a UK Biobank cohort. The method robustly reconstructed a 3 T dataset with field inhomogeneities, including rapid transitions near organ structures.

The full-range PDFF map and the R_2^* map produced by our method are initially magnitude-based. The field map may be estimated more robustly once PDFF and R_2^* have been obtained, provided phase information is available and error-free. It was shown that local minima associated with the phase shift due to the off-resonance frequency of fat are removed when using the proposed method, via demodulation of the water and fat component from the complex-valued raw data. For scanners where obtaining reliable phase images is a challenge, our methodology still enables consistent PDFF and R_2^* estimation, because it is run first via MAGO¹⁸. For this reason, our method may be standardized and deployed across a range of scanning conditions. Indeed, the method may be applied to routinely observed SNR levels from 6-echo datasets at both 1.5 T and 3 T, as shown by the data used in this work, but further validation at high fields is needed.

Smoothness assumptions commonly used by field map regularization in complex-based methodology may not hold true in regions of rapid field variation, which may propagate wrong field map and PDFF estimates to the entire organ of interest (e.g. liver or pancreas). Regularization methods that are initialized using seed pixels in down-sampled data will be particularly sensitive^{7,9}. Slices distanced from the isocenter or closer to the lungs tend to present higher field inhomogeneities, as illustrated by the 3 T dataset. The proposed method produced robust maps under the observed field inhomogeneity range in-vivo, which exceeded 300 Hz at 3 T, suggesting that the proposed method is robust at high fields.

While the proposed field map adjustment step may be considered a form of spatial regularization, note that it is subtly distinct, because instead of smoothing the field map directly, the postprocessed field map at a given voxel comes from the choice of one of the two pre-computed candidate MAGO solutions. Thus, the field map value at a given voxel is derived directly from that voxel's complex-valued raw

data, but it is chosen considering neighboring information. This may avoid issues from previously used spatial regularization, where the field map at a given voxel is forced to assume a value within a pre-defined range, given a combination of field map values from the voxel neighborhood, for example in the interpolation step of region growing⁷. Our approach of choosing from the two candidate MAGO solutions did not seem to penalize rapid field variations and preserved the high-frequency appearance of the field map, where other methods may yield an over-smoothed result.

Note that the field map adjustment step may lead to a chosen MAGO solution set that is not necessarily associated with the lower fitting residual; instead, the solution most consistent with the voxel neighborhood is chosen. This may be useful where noise corrupts the raw data magnitude, causing the physiologically correct solution to become a local optimum. For the refinement of the PDFF and R_2^* estimates, the adjusted field maps could be used to update water and fat using the linearized IDEAL formulation. This would be undesirable as it could propagate phase errors, which would in turn need a magnitude refinement step. This is the reasoning behind hybrid fitting¹⁶. Choosing from the two candidate magnitude-based solutions removed the need for a magnitude-based refinement step.

This work had several limitations. Field map regularization techniques may be used to extend our method's reported range limit, which could limit applicability for QSM. For example, multi-slice data may benefit from additional smoothness constraints applied in the slice direction, as demonstrated previously^{11,13,31}. No 3-D methods were compared in this work, because UK Biobank data was single-slice and we chose to keep the proposed method consistent throughout the experiments. Also, slice-by-slice reconstruction facilitates standardization. Note that future multi-slice extensions could be applied to the 3 T dataset from this work. In this scenario, median filtering may need to be revisited in favor of piece-wise techniques. QSM-specific validation would also be needed under QSM application.

Two different acquisition protocols were evaluated, both with six echoes. The ΔTE was approximately half at 3 T, where the chemical shift is double, therefore the two protocols can be expected to result in similar method performance. It remains unclear how sensitive the proposed method is to acquisition parameters, but the performance of MAGO has been evaluated in phantoms using different acquisition protocols¹⁸. Adjusted R_2^* results were not included in this work, and so future validation work will focus on R_2^* agreement, though MAGO has been validated previously for R_2^* quantification¹⁸.

Conclusions

Our results suggest that magnitude-based water, fat and R_2^* estimation with resolved water-fat ambiguity may be used to robustly estimate a field map from complex-valued raw data, so that B_0 field mapping need not be a critical step for correct water-fat separation, but can improve proton density fat fraction

estimates. This approach for full-range PDFF and field mapping is robust and widely applicable, and showed potential at high field inhomogeneity.

List of Figures

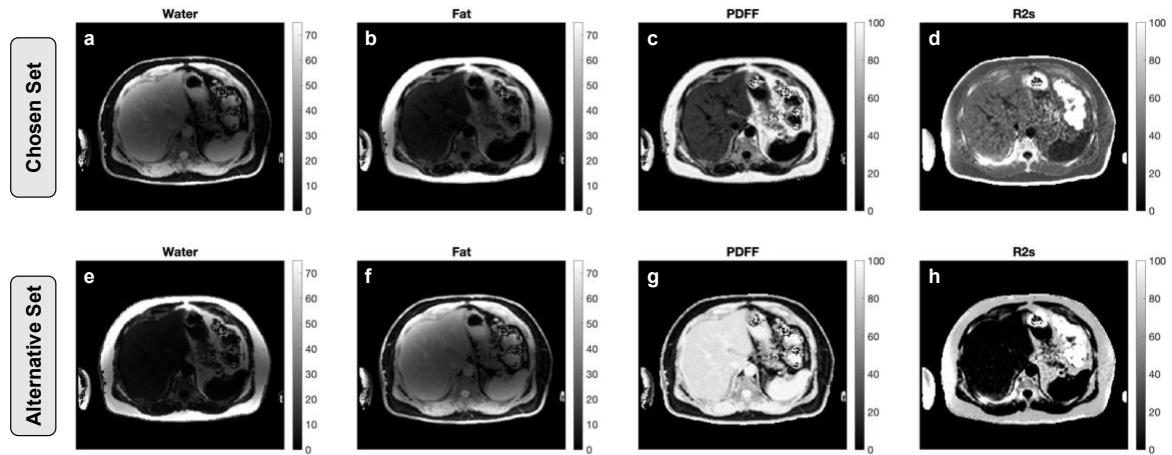


Figure 1. Illustration of magnitude-only fitting with resolved water-fat ambiguity (MAGO). MAGO uses multipoint search to converge to two solution sets, the water-dominant set and the fat-dominant set, where each set contains amounts of water, fat, PDFF and R_2^* . Then chooses, at each voxel, the solution with lowest fitting residual, yielding the chosen solution set (a-d) and the alternative solution set (e-h). This enables PDFF estimation over the full range (0 to 100%) as well as correct R_2^* estimation for the fat-dominant voxels. MAGO, magnitude-only fitting; PDFF, proton density fat fraction

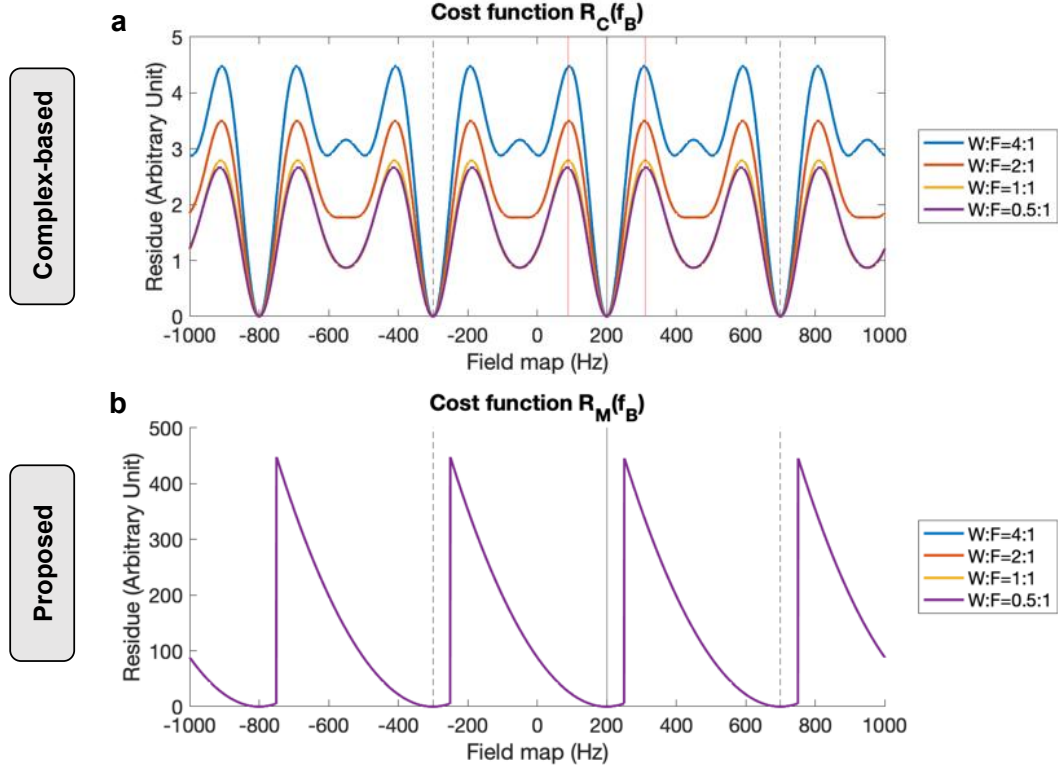


Figure 2. Simulated loss functions for the complex-based estimation problem (a) and for the proposed formulation (b) within a voxel. True field map = 200 Hz (solid grey line), varying voxel Water:Fat proportion, $R_2^* = 30$ Hz, $\phi_0 = 0$ rad, echo times = [2, 4, 6] ms, 1.5 Tesla, 6-peak liver fat spectrum. Voxel-independent complex-based estimation (e.g. IDEAL) converges to an incorrect local minimum near 0 Hz, whereas the proposed voxel-independent method converges to the true value. The proposed loss function is also independent of Water:Fat proportion within the voxel. The period, $\pm 1/\Delta TE$, is marked (dashed lines). True solution $\pm \Delta f/2$ is marked (red lines in a). IDEAL, iterative decomposition of water and fat using echo asymmetry and least squares estimation

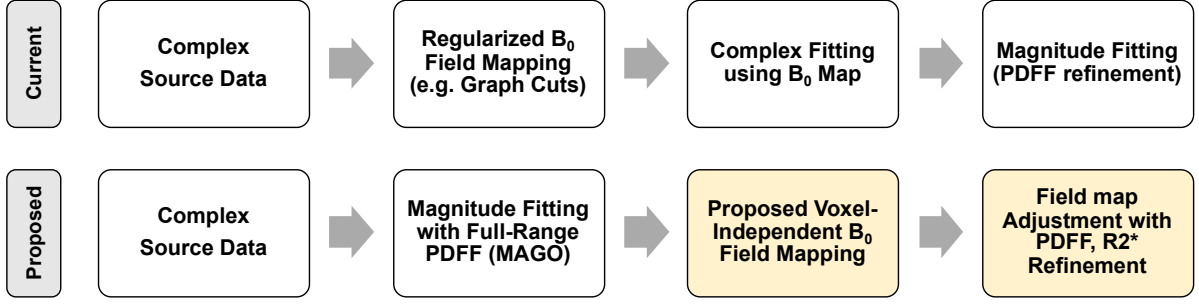


Figure 3. State-of-the-art (top) and proposed (bottom) methods for field mapping and PDF estimation, given complex-valued source data. The yellow modules are those demonstrated in this work. State-of-the-art methods perform field mapping with regularization first, then derive PDFF and R_2^* , and include a final magnitude-based refinement step. The proposed method applies magnitude fitting with resolved water-fat ambiguity (MAGO) first, then performs voxel-independent field mapping, and includes a final adjustment step to refine the MAGO PDFF and R_2^* .

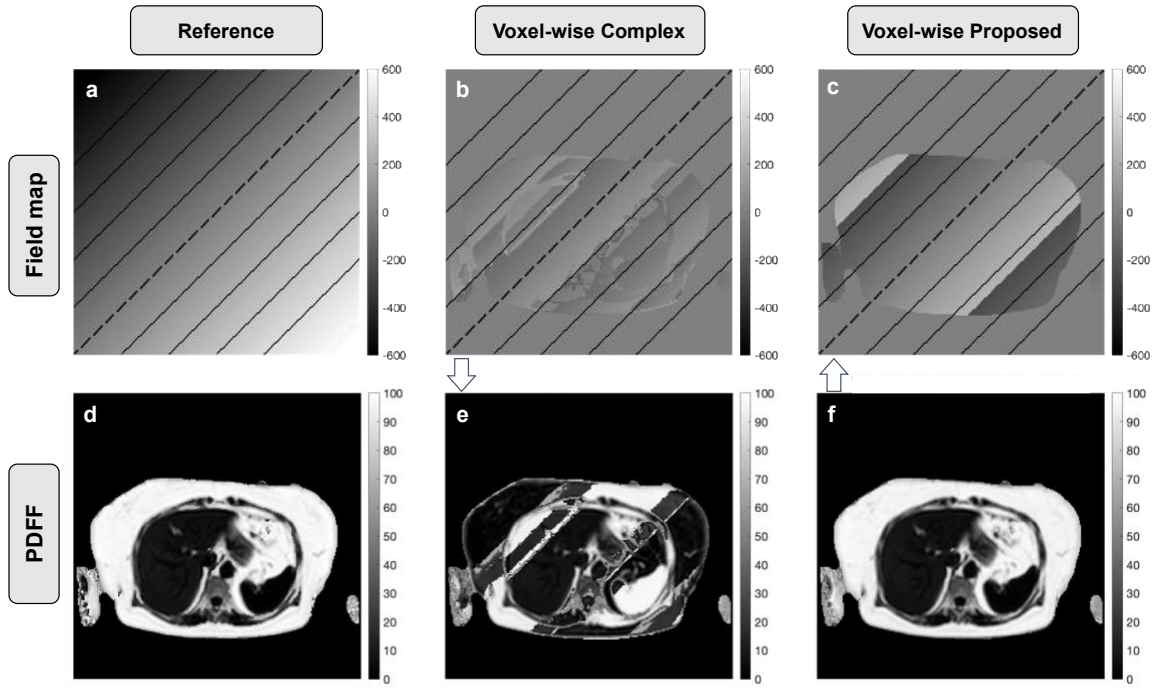


Figure 4. UK Biobank subject with a synthetic field map added. The reference PDFF (a) was obtained using regularized complex-based estimation by GOOSE:hIDEAL prior to adding the synthetic field map (a). Reference field map equal to zero (dashed line, a-c) and reference field map equal to $\pm\Delta f/2$ (solid lines, a-c) are indicated. Voxel-independent hIDEAL (b, e) misconverges beyond $\pm\Delta f/2$. The proposed voxel-independent implementation (c, f) is accurate up to beyond $\pm\Delta f$. Note the wraps in the proposed field map do not affect PDFF, since field map estimation is performed after PDFF is obtained, unlike complex-based methods (dependence indicated by white arrows). GOOSE, fat water decomposition using globally optimal surface estimation; hIDEAL, hybrid IDEAL

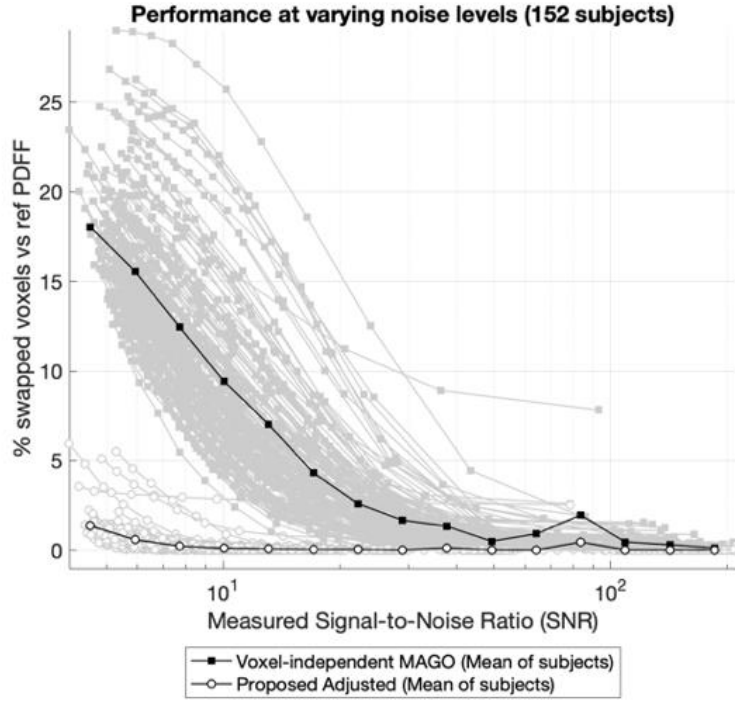


Figure 5. Performance in terms of robustness to noise of the proposed field map adjustment step demonstrated in the UK Biobank population (N=152). For each subject (gray lines), noise was progressively added to the raw data and reconstructed using the proposed voxel-independent method (empty circles) and using the method with the proposed adjustment (filled squares). The number of swapped voxels was determined by comparing the reconstructed PDFF for each method against a reference computed using GOOSE:hIDEAL on the data with no added noise. The number of swapped voxels was plotted against the SNR measured within the liver for that noise step. Mean results across subjects are shown (black lines). SNR, signal-to-noise ratio

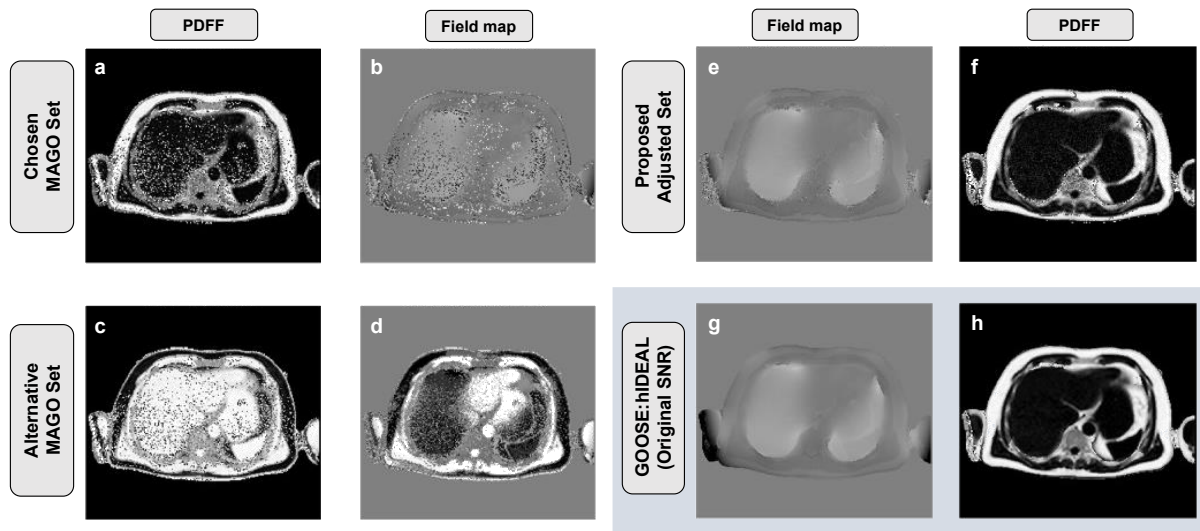


Figure 6. Proposed field map adjustment step on a UK Biobank subject after noise was added to the raw data, yielding $\text{SNR}=10$ within the liver. Results for the proposed voxel-independent method are shown (a, b), corresponding to the chosen MAGO solution set. The proposed adjustment step chooses at each voxel from the chosen MAGO solution (a, b) and the alternative MAGO solution (c, d) by comparing them to a smoothed version of the chosen field map (b). The resulting adjusted field map (e) and PDFF (f) have most voxels corrected using this approach. Reference maps computed by GOOSE:hIDEAL using the original data with no added noise are included for comparison (g, h).

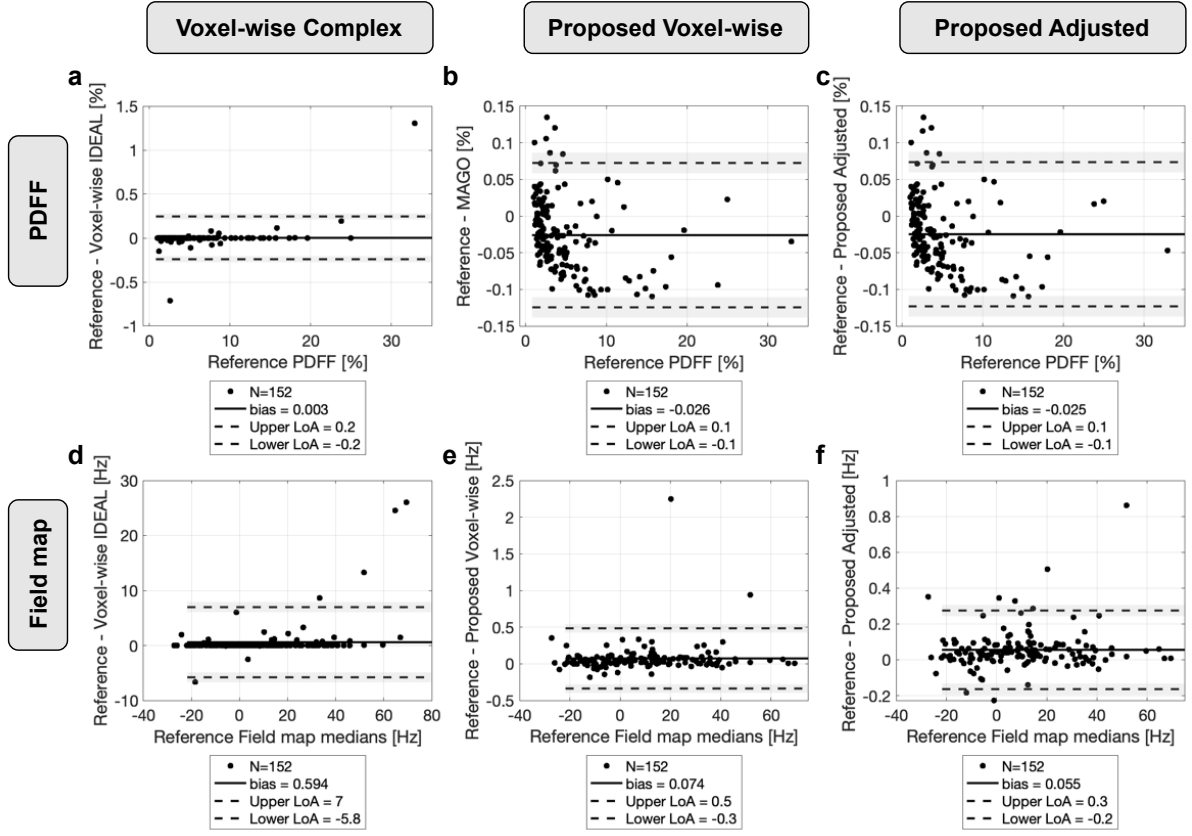


Figure 7. Bland-Altman analysis of reference regularized complex-based estimation by GOOSE:hIDEAL and the proposed methods using the UK Biobank cohort. PDFF (a-c) and Field map (d-f) medians within the liver were extracted. Voxel-independent hIDEAL results (a, d) are shown for comparison. Both proposed methods show agreement with the reference method, with the proposed adjusted method showing higher agreement than the proposed voxel-independent method.

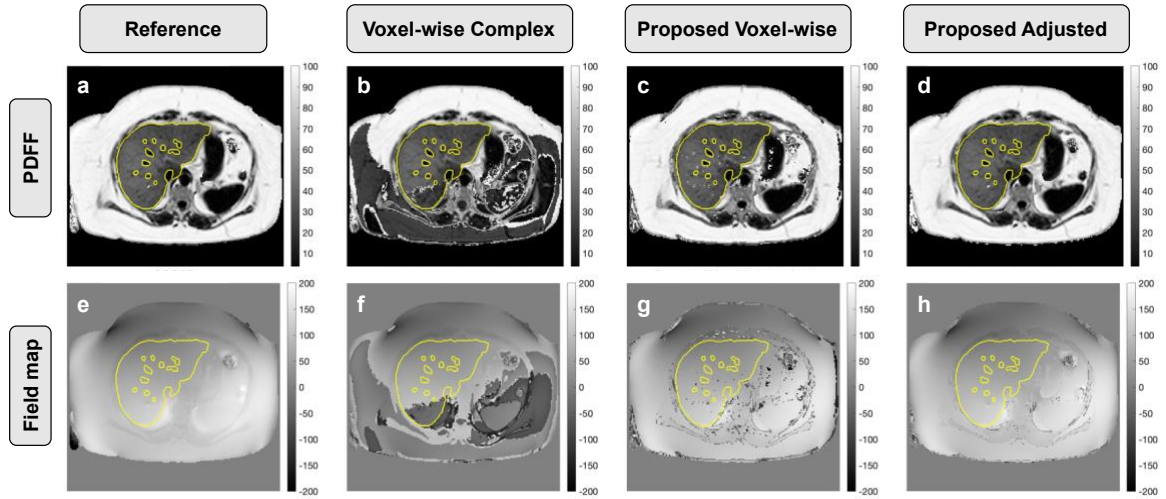


Figure 8. The subject from UK Biobank with highest PDFF disagreement between reference GOOSE:hIDEAL and voxel-independent hIDEAL is shown here reconstructed using GOOSE:hIDEAL (a, e), voxel-independent hIDEAL (b, f), proposed voxel-wise method (c, g) and proposed adjusted method (d, h). Automatic liver segmentations are shown (yellow contours). Voxel-independent hIDEAL suffers from field map aliasing and subsequent fat-water swaps posteriorly within the liver and the surrounding subcutaneous fat. The proposed adjusted method is able to unswap a few voxels within the liver that were misidentified using the proposed voxel-independent method.

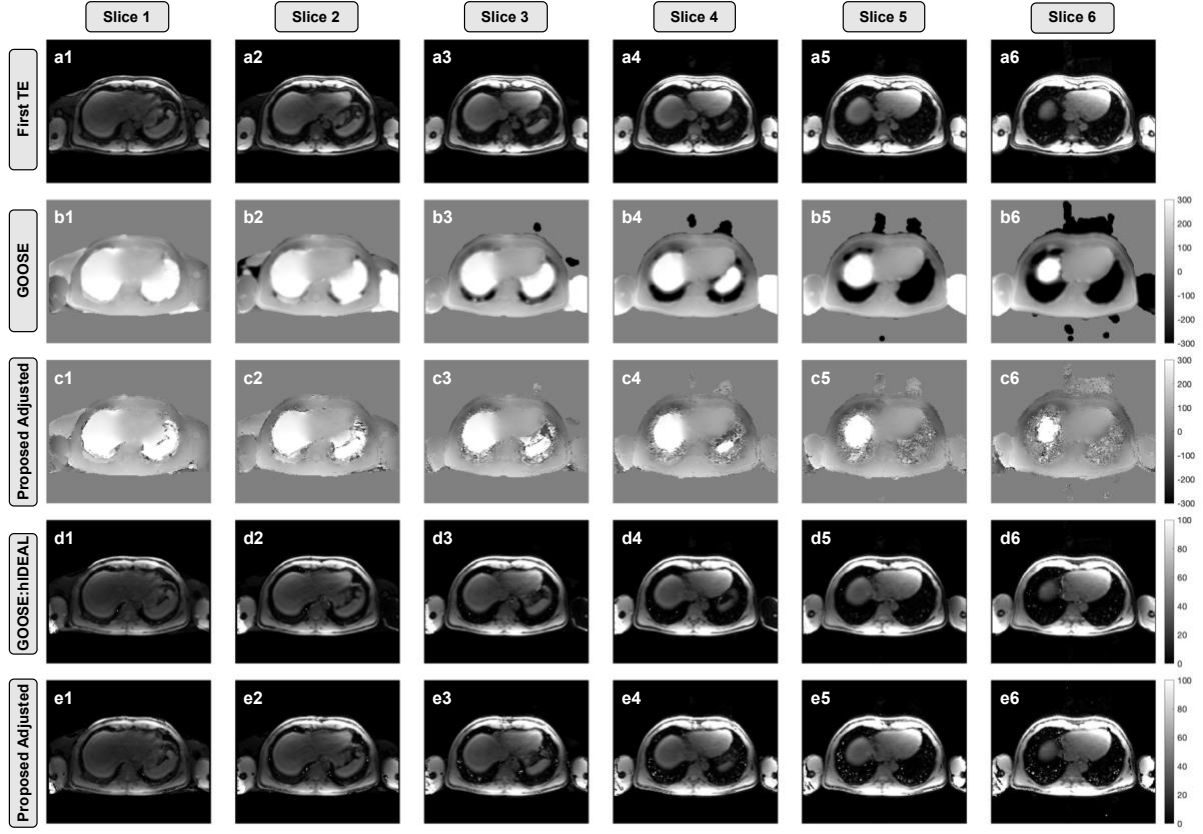


Figure 9. Field map and water-separated images reconstructed from the six of the thirty-two slices from the 3 T dataset that covered the liver. The slices were processed using GOOSE:hIDEAL for reference (b1-b6, d1-d6) and using the proposed adjusted method (c1-c6, e1-e6). Magnitude images from the first echo time are provided for anatomical reference (a1-a6). Regions of high field inhomogeneity and regions of rapid field transitions are observed, especially near the dome of the liver and in the spleen. Both methods were generally in agreement, but some swaps were observed in GOOSE:hIDEAL maps within the subject's left arm (b2-b6), that were not observed for the proposed adjusted method.

Supplementary Material

The 3 T dataset was reconstructed using several widely used methods from the literature for comparison (Fig. S1 and Fig. S2): Region Growing (Yu et al., 2005), Graph Cuts (Hernando et al., 2010), and PRESCO (Bydder et al., 2020). The implementation of Graph Cuts from the Fat-Water Toolbox was run with default parameters, except for the field map search range, that was doubled to $[-800, 800]$ Hz. PRESCO was run with default parameters.

The authors acknowledge the use of the Fat-Water Toolbox for some of the results shown here, available under <http://ismrm.org/workshops/FatWater12/data.htm>, as well as code from Dr Mark Bydder for the PRESCO algorithm, available under <https://github.com/marcsous/pdf>.

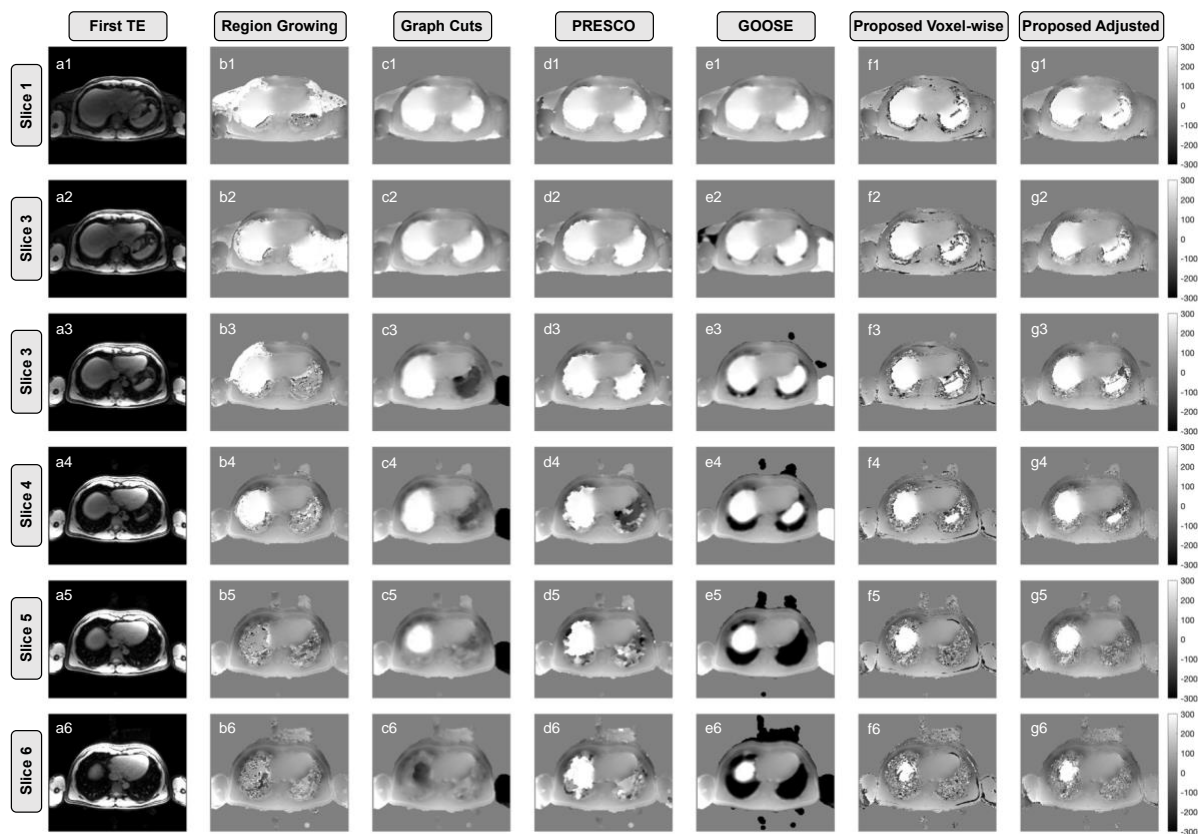


Figure S1. Field maps reconstructed using several widely used methods from the literature. Magnitude images of the first echo time are included for each slice for anatomical reference (a1-a6). Methods used were Region Growing (b1-b6), Graph Cuts (c1-c6), PRESCO (d1-d6), GOOSE (e1-e6), Proposed voxel-wise (f1-f6), Proposed adjusted (g1-g6).

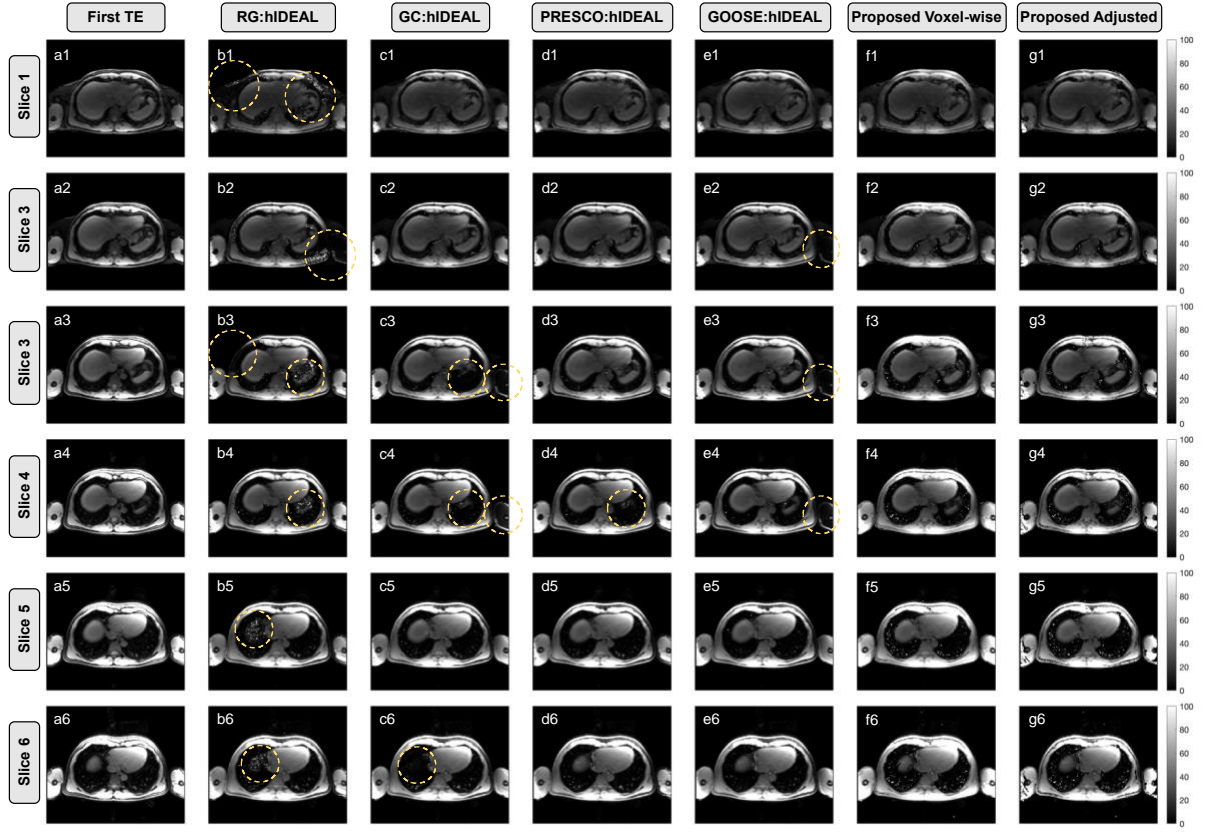


Figure S2. Water-separated maps reconstructed using other widely used methods from the literature. Magnitude images of the first echo time are included for each slice for anatomical reference (a1-a6). Methods used were Region Growing (b1-b6), Graph Cuts (c1-c6), PRESCO (d1-d6), GOOSE (e1-e6), Proposed voxel-wise (f1-f6), Proposed adjusted (g1-g6). Major fat-water swaps are indicated (bright dashed circles).

References

1. Caussy C, Reeder SB, Sirlin CB, Loomba R. Noninvasive, Quantitative Assessment of Liver Fat by MRI-PDFF as an Endpoint in NASH Trials. *Hepatology*. 2018;68(2):763-772. doi:10.1002/hep.29797
2. Franz D, Diefenbach MN, Treibel F, et al. Differentiating supraclavicular from gluteal adipose tissue based on simultaneous PDFF and T2* mapping using a 20-echo gradient-echo acquisition. *Journal of Magnetic Resonance Imaging*. 2019;50(2):424-434. doi:10.1002/jmri.26661
3. Idilman IS, Tuzun A, Savas B, et al. Quantification of liver, pancreas, kidney, and vertebral body MRI-PDFF in non-alcoholic fatty liver disease. *Abdom Imaging*. 2015;40(6):1512-1519. doi:10.1007/s00261-015-0385-0
4. Hernando D, Levin YS, Sirlin CB, Reeder SB. Quantification of liver iron with MRI: State of the art and remaining challenges. *Journal of Magnetic Resonance Imaging*. 2014;40(5):1003-1021. doi:10.1002/jmri.24584
5. Reeder SB, Wen Z, Yu H, et al. Multicoil Dixon Chemical Species Separation with an Iterative Least-Squares Estimation Method. *Magn Reson Med*. 2004;51(1):35-45. doi:10.1002/mrm.10675
6. Hernando D, Haldar JP, Sutton BP, Ma J, Kellman P, Liang ZP. Joint estimation of water/fat images and field inhomogeneity map. *Magn Reson Med*. 2008;59(3):571-580. doi:10.1002/mrm.21522
7. Yu H, Reeder SB, Shimakawa A, Brittain JH, Pelc NJ. Field map estimation with a region growing scheme for iterative 3-point water-fat decomposition. *Magn Reson Med*. 2005;54(4):1032-1039. doi:10.1002/mrm.20654
8. Hernando D, Kellman P, Haldar JP, Liang ZP. Robust water/fat separation in the presence of large field inhomogeneities using a graph cut algorithm. *Magn Reson Med*. 2010;63(1):79-90. doi:10.1002/mrm.22177
9. Lu W, Hargreaves BA. Multiresolution field map estimation using golden section search for water-fat separation. *Magn Reson Med*. 2008;60(1):236-244. doi:10.1002/mrm.21544
10. Fangping Huang, Narayan S, Wilson D, Johnson D, Guo-Qiang Zhang. A Fast Iterated Conditional Modes Algorithm for Water–Fat Decomposition in MRI. *IEEE Trans Med Imaging*. 2011;30(8):1480-1492. doi:10.1109/TMI.2011.2125980

11. Berglund J, Skorpil M. Multi-scale graph-cut algorithm for efficient water-fat separation. *Magn Reson Med*. 2017;78(3):941-949. doi:10.1002/mrm.26479
12. Cui C, Wu X, Newell JD, Jacob M. Fat Water Decomposition Using Globally Optimal Surface Estimation (GOOSE) Algorithm. 2015;1299:1289-1299. doi:10.1002/mrm.25193
13. Boehm C, Diefenbach MN, Makowski MR, Karampinos DC. Improved body quantitative susceptibility mapping by using a variable-layer single-min-cut graph-cut for field-mapping. *Magn Reson Med*. 2021;85(3):1697-1712. doi:10.1002/mrm.28515
14. Hutton C, Gyngell ML, Milanese M, Bagur A, Brady M. Validation of a standardized MRI method for liver fat and T2 quantification. *PLoS One*. 2018;13(9):1-12. doi:10.1371/journal.pone.0204175
15. Bydder M, Yokoo T, Hamilton G, et al. Relaxation effects in the quantification of fat using gradient echo imaging. *Magn Reson Imaging*. 2008;26(3):347-359. doi:10.1016/j.mri.2007.08.012
16. Yu H, Shimakawa A, Hines CDG, et al. Combination of complex-based and magnitude-based multiecho water-fat separation for accurate quantification of fat-fraction. *Magn Reson Med*. 2011;66(1):199-206. doi:10.1002/mrm.22840
17. Yu H, Reeder SB, Shimakawa A, McKenzie CA, Brittain JH. Robust multipoint water-fat separation using fat likelihood analysis. *Magn Reson Med*. 2012;67(4):1065-1076. doi:10.1002/mrm.23087
18. Triay Bagur A, Hutton C, Irving B, Gyngell ML, Robson MD, Brady M. Magnitude-intrinsic water-fat ambiguity can be resolved with multipeak fat modeling and a multipoint search method. *Magn Reson Med*. 2019;82(1):460-475. doi:10.1002/mrm.27728
19. Bray TJ, Bainbridge A, Hall-Craggs MA, Zhang H. MAGORINO: Magnitude-only fat fraction and R2* estimation with Rician noise modelling. Published online October 11, 2021. <http://arxiv.org/abs/2110.05400>
20. Sharma SD, Hernando D, Horng DE, Reeder SB. Quantitative susceptibility mapping in the abdomen as an imaging biomarker of hepatic iron overload. *Magn Reson Med*. 2015;74(3):673-683. doi:10.1002/mrm.25448
21. Hamilton G, Yokoo T, Bydder M, et al. In vivo characterization of the liver fat 1H MR spectrum. *NMR Biomed*. 2011;24(7):784-790. doi:10.1002/nbm.1622

22. Bydder M, Kouzehkonan VG, Gao Y, Robson MD, Yang Y, Hu P. Constraints in estimating the proton density fat fraction. *Magn Reson Imaging*. 2020;66(November 2019):1-8. doi:10.1016/j.mri.2019.11.009
23. Bydder M, Yokoo T, Yu H, Carl M, Reeder SB, Sirlin CB. Constraining the initial phase in water-fat separation. *Magn Reson Imaging*. 2011;29(2):216-221. doi:10.1016/j.mri.2010.08.011
24. Hernando D, Kramer JH, Reeder SB. Multipeak fat-corrected complex R2* relaxometry: Theory, optimization, and clinical validation. *Magn Reson Med*. 2013;70(5):1319-1331. doi:10.1002/mrm.24593
25. Roberts NT, Hernando D, Panagiotopoulos N, Reeder SB. Addressing concomitant gradient phase errors in time-interleaved chemical shift-encoded MRI fat fraction and R 2 * mapping with a pass-specific phase fitting method. *Magn Reson Med*. 2022;(September 2021):1-13. doi:10.1002/mrm.29175
26. Peterson P, Månsson S. Fat quantification using multiecho sequences with bipolar gradients: Investigation of accuracy and noise performance. *Magn Reson Med*. 2014;71(1):219-229. doi:10.1002/mrm.24657
27. Yu H, Shimakawa A, McKenzie CA, Brodsky E, Brittain JH, Reeder SB. Multiecho water-fat separation and simultaneous R*2 estimation with multifrequency fat spectrum modeling. *Magn Reson Med*. 2008;60(5):1122-1134. doi:10.1002/mrm.21737
28. Irving B, Hutton C, Dennis A, et al. Deep quantitative liver segmentation and vessel exclusion to assist in liver assessment. *Communications in Computer and Information Science*. 2017;723:663-673. doi:10.1007/978-3-319-60964-5_58
29. Hernando D, Hines CDG, Yu H, Reeder SB. Addressing phase errors in fat-water imaging using a mixed magnitude/complex fitting method. *Magn Reson Med*. 2012;67(3):638-644. doi:10.1002/mrm.23044
30. Altman DG, Bland JM. Measurement in Medicine: The Analysis of Method Comparison Studies. *The Statistician*. 1983;32(3):307. doi:10.2307/2987937
31. Cui C, Shah A, Wu X, Jacob M. A rapid 3D fat–water decomposition method using globally optimal surface estimation (R-GOOSE). *Magn Reson Med*. 2018;79(4):2401-2407. doi:10.1002/mrm.26843